

Metallized ϵ -FeOOH and the heterogeneous electrical conductivity structure in the lower mantle

Yukai Zhuang (✉ yukai.zhuang@hpstar.ac.cn)

Center for High Pressure Science and Technology Advanced Research <https://orcid.org/0000-0002-5448-6881>

Zhongxun Cui

Center for High Pressure Science and Technology Advanced Research

Ruilian Tang

Center for High Pressure Science and Technology Advanced Research (HPSTAR)

Renbiao Tao

Center for High Pressure Science and Technology Advanced Research

Mingqiang Hou

Carnegie Institution of Washington

Kuo Li

Center for high pressure science and technology advanced research

Jiuhua Chen

Florida International University

Qingyang Hu

Center for High Pressure Science and Technology Advanced Research <https://orcid.org/0000-0002-2742-3017>

Article

Keywords: electrical conductivity, ϵ -FeOOH, lower mantle, insulator-metal transition

Posted Date: August 27th, 2020

DOI: <https://doi.org/10.21203/rs.3.rs-55843/v1>

License:  This work is licensed under a Creative Commons Attribution 4.0 International License.

[Read Full License](#)

Abstract

Electrical heterogeneity at the depth of 900-1400 km in Earth's interior is a key factor to constrain the minor phase composition of the lower mantle. However, prevailing mineralogical models including Fe- or Al-enriched silicates or ferropericlase are insufficient to explain the ultra-high electrical conductivity in local areas of subduction slabs. Here, we measure the electrical conductivity of ϵ -FeOOH up to 61 GPa. A 3-order abrupt jump of electrical conductivity is observed in 45-50 GPa, reaching $1.24 \pm 0.19 \times 10^3$ S/m at 61 GPa. Density mean field theory simulations suggest that ϵ -FeOOH undergoes a Mott-type electronic transition, which leads the conduction mechanism to switch from small polaron conduction to free electron conduction. Compared with bridgmanite, ferropericlase and conventional mantle compositional models, the electrical conductivity of the metallic ϵ -FeOOH is 1-3 orders of magnitude higher. Minor or moderate incorporation of metallic ϵ -FeOOH into the ambient lower mantle could reproduce the observed electrical heterogeneity derived from geomagnetic data at 900-1400 km depth.

Introduction

The lower mantle occupies more than half of the solid Earth by volume. Its mineral composition has attracted enormous research interests as it holds key to understand the Earth's bulk structure, dynamics and physicochemical properties¹. Based on mineral physics experiments, the lower mantle is dominated by bridgmanite (Brg) and ferropericlase (Fp) with a small amount of Ca-perovskite^{2,3}. However, recent seismological measurement⁴, electromagnetic tomography⁵ and deep diamond inclusion⁶ suggest the lower mantle can be locally heterogeneous and thus not fully covered by popular mineralogical models^{2,7}.

Using a combination of global three-dimensional (3D) and one-dimensional (1D) induction studies^{5,8,9,10,11,12}, pioneers have mapped out the electrical conductivity (EC) profiles and have located a couple of areas with very high EC . For example, Constable and Constable constructed a 1-D conductivity model by Occam smooth inversion and showed the EC values surge to 10^2 S/m at around 1300 km depth in the lower mantle¹¹. Those high conductivity regions are observed at depths of 900–1400 km beneath Eastern Africa, South-East Asia and Eurasia in stark contrast to the large low conductivity areas under Australian region, Western Africa, near Japan, North and Central America^{5,12}. The high conductivity number, which is almost two orders of magnitude greater than the mean value, agreed with the 1D conductivity profile obtained with the global earth response and a synthetic 3D model⁵. However, conductivity measurements of Brg or Fp at high pressures indicate that neither Brg nor Fp can reach such high EC values^{13,14,15,16}, even considering temperature effects¹⁷.

As a transport property, EC is mainly controlled by pressure, temperature, oxygen fugacity¹⁸, phase transitions^{14,19,20} and is also sensitive to factors like water solubility²¹ and partial melting²². The large variations of EC in the lower mantle indicate that multiple conductivity mechanisms may co-exist at similar depth. For example, applying high pressure and hydration effect promote the EC of nominal

anhydrous olivine by orders of magnitude due to the onset of proton conduction²³. Wüstite (FeO) enters an exotic metallic state when pressure increases above 70 GPa and temperature is higher than 1900 K²⁴. Those observations provide potential mechanisms to explain the electrical conductivity profiles in the transition zone and the lower mantle.

In this work, we focus on the *EC* of ϵ -FeOOH, a high-pressure phase found to form solid solution with δ -AlOOH and phase H under the CaCl₂-type hydroxide²⁵. FeOOH is also a major component of band iron formations, which were largely subducted with deep ocean during the Archaean era by plate tectonic process²⁶. It is reported that ϵ -FeOOH is a potential water carrier into the deep mantle in the recycled subduction slabs^{27,28}. For its possible minor presence in the lower mantle, we first measured the *EC* of ϵ -FeOOH up to 61 GPa, which is then compared against those of γ -AlOOH (boehmite) and δ -AlOOH to provide a holistic view on the effect of iron. Our *in-situ* measurements indicate that Fe³⁺ in ϵ -FeOOH metalizes at 45–50 GPa and the electronic transition pushes *EC* above 10³ S/m. This is approximately 2 to 2.5 orders of magnitude higher than that of pyrolite or Mid-Ocean Ridge Basalt (MORB) composition and may significantly contribute to the high conductivity observed at the corresponding 900–1400 km depth.

Results

The high-pressure phases of ϵ -FeOOH and δ -AlOOH are synthesized using a large volume multi-anvil press (MAP, see Materials and Methods for details). The pressure-temperature (*P-T*) conditions for MAP experiments are summarized in Table 1. We conducted a set of MAP experiments to synthesize high-pressure samples as well as to constrain the phase stability fields of FeOOH, as shown in Fig. 1. At low pressure (< 7 GPa), FeOOH dehydrates along a steep *P/T* curve^{28,29,30,31}. At higher pressure, our results generally agree with previous MAP results by Yoshino, et al²⁹. Also plotted in Fig. 1 are four different subduction slab geotherms from Kirby et al³². Although the high-pressure ϵ -FeOOH dehydrates at the conditions of mantle geotherm and not considered as a superior stable phase to survive all categories of subducting slabs, it bears the *P-T* conditions of subducting slabs with relatively older age and faster sinking conditions. Once ϵ -FeOOH descends to deeper mantle, it benefits from improved thermal stability (Fig. 1) such that it is capable to carry hydrous and ferric iron enriched fragments deeper. On the other hand, partially dehydrated ϵ -FeOOH may possibly rehydrate in wet local regions of the mantle transition zone³³. Therefore, ϵ -FeOOH is a potential minor phase transporting water down to the lower mantle through cold subducting slabs.

Table 1
Starting samples and products of MAP synthesis.

| Run # | Sample | T (°C) | P (GPa) | Time (minute) | Product |
|-------------|----------|----------|-----------|---------------|-------------------|
| 160314G1127 | Goethite | 600 | 12 | 240 | ϵ -FeOOH |
| 160317G1128 | Goethite | 700 | 12 | 240 | ϵ -FeOOH |
| 160320G1129 | Goethite | 800 | 12 | 240 | ϵ -FeOOH |
| 160411G1135 | Goethite | 900 | 12 | 120 | Hematite |
| 160414G1136 | Goethite | 900 | 14 | 120 | ϵ -FeOOH |
| 160417G1137 | Goethite | 1000 | 14 | 120 | Hematite |

We perform our high-pressure *EC* experiments using impedance spectroscopy at ambient temperature and up to 61 GPa for ϵ -FeOOH (Fig. 2, Table 2). Parallel experiments of δ -AlOOH and γ -AlOOH are performed up to 53 GPa to study the effects of Fe^{3+} . Throughout the experiments, the errors of resistances in the Nyquist plot fitting are less than 1% (Table 2). The high-pressure *in situ EC* numbers are calculated by the van der Pauw method³⁴ (Details in Methods). In Fig. 2, the *EC* of γ -AlOOH is almost invariantly correlated with pressure, while those of γ -AlOOH and ϵ -FeOOH climb with pressure. Specifically, the *EC* of ϵ -FeOOH exhibits an abrupt jump at ~ 45 GPa and reaches $1.24 \pm 0.19 \times 10^3$ S/m at 61.2 GPa. We note that a similar trend of change is also observed in goethite α -FeOOH within similar pressure range^{35,36}. In contrast, the *EC* of γ -AlOOH shows a small kink between 30 and 40 GPa but the increment of *EC* is less than one order of magnitude.

Table 2
EC numbers of ϵ -FeOOH at ambient temperature.

| Pressure (GPa) | Resistance (Ω) | Thickness (μm) | Conductivity σ (S/m) | Conductivity $\text{Log}_{10}[\sigma(\text{S/m})]$ |
|----------------|-------------------------|-----------------------------|--------------------------------|--|
| 0.3(1) | $4.7(3) \times 10^5$ | 74.1(148) | $6.26(93) \times 10^{-3}$ | -2.20 |
| 4.5(5) | $4.0(1) \times 10^5$ | 62.0(123) | $8.67(13) \times 10^{-3}$ | -2.06 |
| 8.1(8) | $3.5(2) \times 10^5$ | 52.6(105) | $1.18(17) \times 10^{-2}$ | -1.92 |
| 10.7(10) | $3.0(1) \times 10^5$ | 46.4(92) | $1.57(23) \times 10^{-2}$ | -1.80 |
| 15.1(15) | $2.1(2) \times 10^5$ | 36.9(74) | $2.75(41) \times 10^{-2}$ | -1.56 |
| 18.4(18) | $1.5(1) \times 10^5$ | 30.7(61) | $4.54(68) \times 10^{-2}$ | -1.34 |
| 23.1(21) | $1.1(1) \times 10^5$ | 23.2(46) | $8.01(12) \times 10^{-2}$ | -1.09 |
| 25.7(24) | $1.1(2) \times 10^5$ | 19.7(39) | $9.92(14) \times 10^{-2}$ | -1.00 |
| 28.1(31) | $1.0(3) \times 10^5$ | 16.9(33) | $1.25(18) \times 10^{-1}$ | -0.90 |
| 30.5(33) | $9.7(3) \times 10^4$ | 14.5(29) | $1.55(23) \times 10^{-1}$ | -0.80 |
| 32.3(35) | $9.0(2) \times 10^4$ | 13.0(26) | $1.86(27) \times 10^{-1}$ | -0.72 |
| 34.7(38) | $8.1(1) \times 10^4$ | 11.3(22) | $2.39(35) \times 10^{-1}$ | -0.62 |
| 37.5(41) | $7.2(1) \times 10^4$ | 9.84(19) | $3.09(46) \times 10^{-1}$ | -0.50 |
| 40.9(44) | $6.2(2) \times 10^4$ | 8.8(17) | $3.96(59) \times 10^{-1}$ | -0.40 |
| 43.7(48) | $5.4(3) \times 10^4$ | 8.6(17) | $4.70(61) \times 10^{-1}$ | -0.32 |
| 46.1(52) | $9.2(2) \times 10^2$ | 8.4(17) | $2.78(41) \times 10^1$ | 1.44 |
| 50.7(55) | $1.2(3) \times 10^2$ | 8.4(17) | $2.08(31) \times 10^2$ | 2.31 |
| 53.3(58) | $6.4(1) \times 10^1$ | 8.3(16) | $4.10(63) \times 10^2$ | 2.61 |
| 56.1(61) | $4.3(1) \times 10^1$ | 8.2(16) | $6.03(87) \times 10^2$ | 2.78 |
| 61.2(67) | $2.2(3) \times 10^1$ | 8.0(15) | $1.24(19) \times 10^3$ | 3.09 |

Figure 3 showed representative Nyquist plots of ϵ -FeOOH up to 61.7 GPa. The plots are fitted with the Z-View software³⁷ and the fitting errors are generally less than 1%. Up to 53.5 GPa, only one semi-circle exists in the high frequency region (inset in Fig. 3a). Below 45 GPa, ϵ -FeOOH is well defined as an

insulating phase. It has the same small polaron hopping conduction as many other insulating hydroxide or hydrous minerals³⁸. At 53.5 GPa, a second semi-circular arc appears in the low frequency region next to the main circle (Fig. 3b). The onset of the second arc is often attributed to grain boundary resistance³⁹. This is previously regarded as a symbol of anisotropy of the charge carrier transportation in the crystallites⁴⁰. While both our x-ray diffraction experiment and literature data indicate that ϵ -FeOOH is a stable phase throughout the pressure range we have investigated^{27, 41, 42}, the appearance of the second arc coincides with the spin-paring of Fe⁴². The spin transition of Fe may create grain boundaries between the high-spin and low-spin domains. Above the critical pressure, the *EC* of ϵ -FeOOH sharply increases and is comparable to metal, for example the metallic FeO²⁴ and FeH⁴³. Upon further compression, the arc at the low-frequency region becomes insignificant while the high-frequency arc dominates. Such wax and wane imply the progression of spin transition. From 53.5 to 61.7 GPa, it is possible to have two conduction mechanisms competing with each other.

In Fig. 3c, we calculate the relationship between pressure and relaxation frequency for the conduction of grain and grain boundary by fitting the impedance spectra with an equivalent-circuit method (Fig. 3a, 3b insert)⁴⁴. The characteristic relaxation frequency (f) can be obtained by the equivalent circuit model of a constant phase element (CPE) using the equations⁴⁵:

$$f = 1/(2\pi RC)$$

where R is the resistance (intercept of the semiarc with the imaginary axis); C is the capacitance, $C = (Rt)^{1/H}/R$ (t is a fitting parameter that equals to the capacitance of the CPE when it behaves as an ideal capacitor and H is a value between 0 and 1 depending on the suppression angle of the semi-circle). Similar to *EC*, f gradually increases with the compression and spikes at 40–45 GPa due to the electronic transition of Fe. At about 52 GPa, f for grain interior significantly drops and that for grain boundary emerges. This is consistent with measured *EC* value which soars at the same pressure range. The low-spin configuration may play a significant role in the high *EC*.

We conducted first-principles simulation to study the underlying electronic transition. For the strong-correlated system of simple iron-oxide, it is technically challenging to accurately reproduce their electronic structures⁴⁶. A previous study on the pyrite-type FeO₂H_x indicated neither conventional density function theory (DFT) nor DFT with Hubbard correction can fully describe its electronic structure⁴⁷. Hence, we performed comprehensive DFT + density mean-field theories (DMFT) calculation for ϵ -FeOOH. This method was successfully implemented to FeO₂ and FeO₂H^{48, 49}. We started with DFT calculations, which gave fully relaxed structures with volumes corresponding to 1 bar, 30 GPa and 50 GPa respectively. Then both Fe 3*d* and O 2*p* orbitals are wannierized in the energy window from - 11 eV to 5 eV (with the Fermi level at 0 eV). We then solve the quantum impurity problem in DMFT by a continuous-time hybridization expansion solver (details in Methods).

In Fig. 4, the Fermi level comes across the valence band when unit cell volume is below 51.27 \AA^3 , which is a clear evidence of metallization (band structures in Supplementary Fig. 1–3). The metallization is mainly associated with Fe *d* orbitals and the Fermi level shifts to the valence bands. This is due to the weakening of the Mott-Hubbard energy. Thermal fluctuations between the high-spin and low-spin states of Fe^{3+} trigger the insulator-metal transition. The same transition mechanism is also found in BiFeO_3 , which carries ferric iron⁵⁰. It is worth noting that the metallic $\varepsilon\text{-FeO}_2\text{H}$ is in the low-spin configuration. Consequently, for low-spin $\varepsilon\text{-FeOOH}$, small-polaron hopping model converts to the free electron model that is often found in metal.

Discussion

The jump of *EC* is absent in Al endmember $\gamma\text{-AlOOH}$ or $\delta\text{-AlOOH}$ up to 55 GPa. This is reasonable since Al atom has no *d* electrons in the valence band, thus is unlikely to metalize through a spin transition (Fig. 2). Similar to the incorporation of Mg to wüstite, adding Al to $\varepsilon\text{-FeOOH}$ is expected to scale down the *EC* changes during electronic transition. Here, our results on the end members may bracket the upper and lower limits of *EC*.

For the large-scale electrical structure of the lower mantle, a more comprehensive mineral system should be taken into account. In Fig. 5, we compare the *EC* of $\varepsilon\text{-FeOOH}$ with a variety of lower mantle components including Brg, Fp, and mineral phases in MORB compositional model. Also plotted in Fig. 5 are the high and average 1D *EC* profile from frequency dependent impedance response functions of the geomagnetic field by Constable and Constable¹¹ and Ohta et al.⁵¹, respectively. When pressure is below 45 GPa, *EC* numbers from the majority of mineral phases are varying within a modest 1–2 orders of magnitude. One exception is the semiconducting wüstite which leaves a significant gap with other compositions. The mineralogy data is generally consistent with geomagnetic models which regard the top later of the lower mantle is relatively homogeneous⁵. Crossing the transition point at 45 GPa, the *EC* of $\varepsilon\text{-FeOOH}$ shoots up by 3 orders of magnitude due to metallization. Triggered by a Mott-type insulator to metal transition, the *EC* jump observed in $\varepsilon\text{-FeOOH}$ at 45 GPa is distinct from other lower mantle minerals. Comparing with other ferric system, for instances the $\text{Mg}_{0.83}\text{Fe}_{0.21}\text{Al}_{0.06}\text{Si}_{0.91}\text{O}_3$ Brg¹³ and $\text{Mg}_{0.60}\text{Fe}_{0.40}\text{Si}_{0.63}\text{Al}_{0.37}\text{O}_3$ Brg⁵² silicates, the increment of *EC* is only moderate and approximately monotonous with pressure without dramatic jumps. Otherwise, the high to low-spin transition of ferrous iron slows the mobility of the charge transfer carriers of low-spin Fe^{2+} , thus lowers *EC*¹⁴. In the cases of $(\text{Mg}_{0.75}\text{Fe}_{0.25})\text{O}^{14}$, $(\text{Mg}_{0.81}\text{Fe}_{0.19})\text{O}^{53}$, and $(\text{Mg}_{0.9}\text{Fe}_{0.1})\text{SiO}_3$ Brg⁵⁴, spin transition reduces total *EC* by ~ 0.5 -1 orders across the transition point. In short, the metallization pressure in $\varepsilon\text{-FeOOH}$ matches the pressure of significant step increase in the 1D *EC* profile reported by Constable and Constable¹¹ (Fig. 5). The divergence of *EC* in different mineral phases above 45 GPa may give rise to the lateral conductivity heterogeneity in the deep lower mantle due to their chemical (phase) heterogeneity. While the major components of the lower mantle like Brg and Fp feature low *EC* in their insulating phases, $\varepsilon\text{-FeOOH}$ is

among the few phases to establish significantly higher *EC*. ϵ -FeOOH, owing to the electronic transition, would be a candidate to explain the electrically heterogeneous lower mantle.

In Fig. 6, we overlay a synthetic 3D conductivity structure⁵ at 1220 km depth on a map of tectonic plates in the South China Sea region⁵⁷. The separation of high *EC* and low *EC* regions have an intriguing relation with the plot of tectonic plates. A large portion of the high *EC* regions are located at the stagnant slab beneath subduction zones, which is enriched in water and ferric iron^{58, 59}. Mineral physics experiments also support the concentration of Fe³⁺ and water content is positively correlated³³. We also notice in some local regions, the *EC* values may surge to the level of 10² S/m, which is not fully covered by the highly conductive mid-oceanic ridge basalt (MORB) segments. Here, we assume a scenario of mixing ϵ -FeOOH to a MORB composition at the bottom of subduction slabs. Using the simple averaging theorem⁶⁰, mixing 25% of ϵ -FeOOH to a MORB composition yields a total *EC* of 18.1 ± 2.7 S/m at 50 GPa. This is 7 times higher than the average *EC* profile shown in Fig. 5 and in line with the higher variation of electrical heterogeneity estimated by the 3D synthetic model⁵ in the range of 1200–1400 km depth, *e.g.* at the Java subduction slab^{61, 62} (Fig. 6). In addition, when hydrous ϵ -FeOOH meets hotter regions in the mantle, it causes dehydration melting that would further boost the overall transport properties⁶³. We therefore suggest that those localized domains with topped 10² S/m *EC* may have incorporated higher concentration of ϵ -FeOOH, or the enrichment of other superior *EC* components.

To sum up, high pressure alters the electron conduction mechanism in ϵ -FeOOH from insulator to metal at about 45 GPa. This transition is accompanied with a nearly 3 orders of magnitude increase in *EC*. The metallic ϵ -FeOOH has much higher *EC* than major lower mantle compositions. Minor to moderate presence of the metallic ϵ -FeOOH causes the overall *EC* in a conventional mineral assemblage to approach the high *EC* profiles of the lower mantle⁵⁷, giving rise to a possible *EC* heterogeneity in the deep lower mantle. Future studies of seismology and deep diamond inclusions are on-demand to detect and constrain the availability of iron-enriched hydrous materials in the lower mantle.

References

1. Wicks, J. K. & Duffy, T. S. Crystal Structures of Minerals in the Lower Mantle. In: *In deep Earth* (eds Terasaki H, Fischer RA). American Geophysical Union (2016).
2. Murakami, M., Ohishi, Y., Hirao, N. & Hirose, K. A perovskitic lower mantle inferred from high-pressure, high-temperature sound velocity data. *Nature* **485**, 90-94 (2012).
3. Kesson, S. E., Fitz Gerald, J. D. & Shelley, J. M. Mineralogy and dynamics of a pyrolite lower mantle. *Nature* **393**, 252-255 (1998).
4. McNamara, A. K., Garnero, E. J. & Rost, S. Tracking deep mantle reservoirs with ultra-low velocity zones. *Earth Planet. Sci. Lett.* **299**, 1-9 (2010).
5. Tarits, P. & Mandéa, M. The heterogeneous electrical conductivity structure of the lower mantle. *Phys. Earth Planet. Inter.* **183**, 115-125 (2010).

6. Tschauner, O. et al. Ice-VII inclusions in diamonds: Evidence for aqueous fluid in Earth's deep mantle. *Science* **359**, 1136-1139 (2018).
7. Ricolleau, A. et al. Density profile of pyrolite under the lower mantle conditions. *Geophys. Res. Lett.* **36**, L06302 (2009).
8. Kelbert, A., Schultz, A. & Egbert, G. Global electromagnetic induction constraints on transition-zone water content variations. *Nature* **460**, 1003-1006 (2009).
9. Utada, H., Koyama, T., Obayashi, M. & Fukao, Y. A joint interpretation of electromagnetic and seismic tomography models suggests the mantle transition zone below Europe is dry. *Earth Planet. Sci. Lett.* **281**, 249-257 (2009).
10. Utada, H., Koyama, T., Shimizu, H. & Chave, A. D. A semi-global reference model for electrical conductivity in the mid-mantle beneath the north Pacific region. *Geophys. Res. Lett.* **30**, 43 (2003).
11. Constable, S. & Constable, C. Observing geomagnetic induction in magnetic satellite measurements and associated implications for mantle conductivity. *Geochemistry, Geophys. Geosystems* **5**, Q01006 (2004).
12. Kuvshinov, A. & Olsen, N. A global model of mantle conductivity derived from 5 years of CHAMP, Ørsted, and SAC-C magnetic data. *Geophys. Res. Lett.* **33**, L18301 (2006).
13. Sinmyo, R., Pesce, G., Greenberg, E., McCammon, C. & Dubrovinsky, L. Lower mantle electrical conductivity based on measurements of Al, Fe-bearing perovskite under lower mantle conditions. *Earth Planet. Sci. Lett.* **393**, 165-172 (2014).
14. Lin, J.-F. et al. Electrical conductivity of the lower-mantle ferropericlase across the electronic spin transition. *Geophys. Res. Lett.* **34**, L16305 (2007).
15. Xu, Y., Shankland, T. J. & Poe, B. T. Laboratory-based electrical conductivity in the Earth's mantle. *J. Geophys. Res. Solid Earth* **105**, 27865-27875 (2000).
16. Shankland, T. J., Peyronneau, J. & Poirier, J.-P. Electrical conductivity of the Earth's lower mantle. *Nature* **366**, 453-455 (1993).
17. Katsura, T., Sato, K. & Ito, E. Electrical conductivity of silicate perovskite at lower-mantle conditions. *Nature* **395**, 493-495 (1998).
18. Karato, S.-i. & Wang, D. Electrical conductivity of minerals and rocks. In: *Physics and chemistry of the deep Earth* (ed Karato S-i) (2013).
19. Greenberg, E. et al. Pressure-induced site-selective Mott insulator-metal transition in Fe₂O₃. *Phys. Rev. X* **8**, 031059 (2018).
20. Potapkin, V. et al. Effect of iron oxidation state on the electrical conductivity of the Earth's lower mantle. *Nat. Commun.* **4**, 1427 (2013).
21. Yoshino, T. & Katsura, T. Electrical conductivity of mantle minerals: Role of water in conductivity anomalies. *Annu. Rev. Earth Planet. Sci.* **41**, 605-628 (2013).
22. Li, Z., Li, J., Lange, R., Liu, J. & Militzer, B. Determination of calcium carbonate and sodium carbonate melting curves up to Earth's transition zone pressures with implications for the deep carbon cycle.

- Earth Planet. Sc. Lett.* **457**, 395-402 (2017).
23. Wang, D., Mookherjee, M., Xu, Y. & Karato, S.-i. The effect of water on the electrical conductivity of olivine. *Nature* **443**, 977-980 (2006).
 24. Ohta, K., Cohen, R. E., Hirose, K., Haule, K., Shimizu, K. & Ohishi, Y. Experimental and theoretical evidence for pressure-induced metallization in FeO with rocksalt-type structure. *Phys. Rev. Lett.* **108**, 026403 (2012).
 25. Nishi, M. et al. Solid Solution and Compression Behavior of Hydroxides in the Lower Mantle. *J. Geophys. Res. Solid Earth* **124**, 10231-10239 (2019).
 26. Lascelles, D. F. Plate tectonics caused the demise of banded iron formations. *Appl. Earth Sci.. Trans. Inst. Min. Metall. B* **122**, 230-241 (2014).
 27. Thompson, E. C., Campbell, A. J. & Tsuchiya, J. Elasticity of ϵ -FeOOH: Seismic implications for Earth's lower mantle. *J. Geophys. Res. Solid Earth* **122**, 5038-5047 (2017).
 28. Nishihara, Y. & Matsukage, K. N. Iron-titanium oxyhydroxides as water carriers in the Earth's deep mantle. *Am. Miner.* **101**, 919-927 (2016).
 29. Yoshino, T., Baker, E. & Duffey, K. Fate of water in subducted hydrous sediments deduced from stability fields of FeOOH and AlOOH up to 20 GPa. *Phys. Earth Planet. Inter.* **294**, 106295 (2019).
 30. Gleason, A. E., Jeanloz, R. & Kunz, M. Pressure-temperature stability studies of FeOOH using X-ray diffraction. In: *Am. Miner.* (2008).
 31. Voigt, R. & Will, G. The system $\text{Fe}_2\text{O}_3\text{-H}_2\text{O}$ under high pressure. *Neues Jahr. für Mineral.* **2**, 89-96 (1981).
 32. Kirby, S. H., Stein, S., Okal, E. A. & Rubie, D. C. Metastable mantle phase transformations and deep earthquakes in subducting oceanic lithosphere. *Rev. Geophys.* **34**, 261-306 (1996).
 33. McCammon, C. A. et al. Oxidation state of iron in hydrous mantle phases: implications for subduction and mantle oxygen fugacity. *Phys. Earth Planet. Inter.* **143-144**, 157-169 (2004).
 34. van der Pauw, L. J. A method of measuring specific resistivity and Hall effect of discs of arbitrary shape. *Philips Res. Repts* **13**, 1-9 (1958).
 35. Xu, W. et al. Pressure-induced hydrogen bond symmetrization in iron oxyhydroxide. *Phys. Rev. Lett.* **111**, 175501 (2013).
 36. Tang, R. et al. Study on the High-Pressure Behavior of Goethite up to 32 GPa Using X-Ray Diffraction, Raman, and Electrical Impedance Spectroscopy. *Minerals* **10**, 99 (2020).
 37. Johnson, D. ZView: a software program for IES analysis, version 2.8. *Scribner Associates, Inc., Southern Pines, NC*, 200 (2002).
 38. Kaneko, K., Inoue, N. & Ishikawa, T. Electrical and photoadsorptive properties of valence-controlled α -iron hydroxide oxide. *J. Phys. Chem.* **93**, 1988-1992 (1989).
 39. Zhuang, Y. et al. Pressure-induced permanent metallization with reversible structural transition in molybdenum disulfide. *Appl. Phys. Lett.* **110**, 122103 (2017).

40. Wang, L. et al. Effect of crystallization water on the structural and electrical properties of CuWO_4 under high pressure. *Appl. Phys. Lett.* **107**, 201603 (2015).
41. Zhuang, Y., Cui, Z., Zhang, D., Liu, J., Tao, R. & Hu, Q. Experimental Evidence for Partially Dehydrogenated $\epsilon\text{-FeOOH}$. *Crystals* **9**, 356 (2019).
42. Gleason, A. E., Quiroga, C. E., Suzuki, A., Pentcheva, R. & Mao, W. L. Symmetrization driven spin transition in $\epsilon\text{-FeOOH}$ at high pressure. *Earth Planet. Sc. Lett.* **379**, 49-55 (2013).
43. Matsuoka, T., Hirao, N., Ohishi, Y., Shimizu, K., Machida, A. & Aoki, K. Structural and electrical transport properties of FeH_x under high pressures and low temperatures. *High Press. Res.* **31**, 64-67 (2011).
44. Dittrich, T., Weidmann, J., Koch, F., Uhlendorf, I. & Laueremann, I. Temperature- and oxygen partial pressure-dependent electrical conductivity in nanoporous rutile and anatase. *Appl. Phys. Lett.* **75**, 3980-3982 (1999).
45. MacDonald, J. R. *Impedance Spectroscopy—Emphasizing Solid Materials and Systems*. Wiley-Interscience, John Wiley and Sons (1987).
46. Lu, C. & Chen, C. High-Pressure Evolution of Crystal Bonding Structures and Properties of FeOOH . *J. Phys. Chem. Lett.* **9**, 2181-2185 (2018).
47. Shorikov, A. O., Poteryaev, A. I., Anisimov, V. I. & Streltsov, S. V. Hydrogenation-driven formation of local magnetic moments in FeO_2H_x . *Phys. Rev. B* **98**, 165145 (2018).
48. Streltsov, S. S., Shorikov, A. O., Skornyakov, S. L., Poteryaev, A. I. & Khomskii, D. I. Unexpected 3+ valence of iron in FeO_2 , a geologically important material lying "in between" oxides and peroxides. *Sci. Rep.* **7**, 13005 (2017).
49. Jang, B. G. et al. Electronic spin transition in FeO_2 : Evidence for Fe(II) with peroxide O_2^{2-} . *Phys. Rev. B* **100**, 014418 (2019).
50. Gavriluk, A. G., Struzhkin, V. V., Lyubutin, I. S., Ovchinnikov, S. G., Hu, M. Y. & Chow, P. Another mechanism for the insulator-metal transition observed in Mott insulators. *Phys. Rev. B* **77**, 155112 (2008).
51. Ohta, K., Hirose, K., Ichiki, M., Shimizu, K., Sata, N. & Ohishi, Y. Electrical conductivities of pyrolitic mantle and MORB materials up to the lowermost mantle conditions. *Earth Planet. Sci. Lett.* **289**, 497-502 (2010).
52. Potapkin, V. et al. Effect of iron oxidation state on the electrical conductivity of the Earth's lower mantle. *Nat. Commun.* **4**, 1427 (2013).
53. Ohta, K., Hirose, K., Onoda, S. & Shimizu, K. The effect of iron spin transition on electrical conductivity of $(\text{Mg,Fe})\text{O}$ magnesiowüstite. *Proc. Jpn. Acad., Ser. B* **83**, 97-100 (2007).
54. Ohta, K., Hirose, K., Shimizu, K., Sata, N. & Ohishi, Y. The electrical resistance measurements of $(\text{Mg,Fe})\text{SiO}_3$ perovskite at high pressures and implications for electronic spin transition of iron. *Phys. Earth Planet. Inter.* **180**, 154-158 (2010).

55. Liu, J. et al. Valence and spin states of iron are invisible in Earth's lower mantle. *Nat. Commun.* **9**, 1284 (2018).
56. Ohta, K., Hirose, K., Shimizu, K. & Ohishi, Y. High-pressure experimental evidence for metal FeO with normal NiAs-type structure. *Phys. Rev. B* **82**, 174120 (2010).
57. Goes, S., Agrusta, R., van Hunen, J. & Garel, F. Subduction-transition zone interaction: A review. *Geosphere* **13**, 644-664 (2017).
58. Lee, C.-T., Lee, T. & Wu, C.-T. Modeling the compositional evolution of recharging, evacuating, and fractionating (REFC) magma chambers: Implications for differentiation of arc magmas. *Geochim. Cosmochim. Acta* **143**, 8–22 (2014).
59. Wang, X., Tsuchiya, T. & Hase, A. Computational support for a pyrolitic lower mantle containing ferric iron. *Nat. Geosci.* **8**, 556-559 (2015).
60. Deschamps, F. & Khan, A. Electrical conductivity as a constraint on lower mantle thermo-chemical structure. *Earth Planet. Sci. Lett.* **450**, 108-119 (2016).
61. Fukao, Y., Widiyantoro, S. & Obayashi, M. Stagnant slabs in the upper and lower mantle transition region. *Rev. Geophys.* **39**, 291-323 (2001).
62. Hall, R. & Spakman, W. Mantle structure and tectonic history of SE Asia. *Tectonophysics* **658**, 14-45 (2015).
63. Laumonier, M. et al. Experimental determination of melt interconnectivity and electrical conductivity in the upper mantle. *Earth Planet. Sci. Lett.* **463**, 286-297 (2017).
64. Li, M. et al. Thickness measurement of sample in diamond anvil cell. *Rev. Sci. Instrum.* **78**, 075106 (2007).
65. Giannozzi, P. et al. Advanced capabilities for materials modelling with Quantum ESPRESSO. *J. Phys.: Condens. Matter* **29**, 465901 (2017).
66. Korotin, D. et al. Construction and solution of a Wannier-functions based amiltonian in the pseudopotential plane-wave framework for strongly orrelated materials. *Eur. Phys. J. B* **65**, 91 (2008).
67. Parcollet, O. et al. TRIQS: A toolbox for research on interacting quantum systems. *Comput. Phys. Commun.* **196**, 398-415 (2015).
68. Werner, P., Comanac, A., de' Medici, L., Troyer, M. & Millis, A. J. Continuous-Time Solver for Quantum Impurity Models. *Phys. Rev. Lett.* **97**, 076405 (2006).
69. Shinaoka, H., Nomura, Y. & Gull, E. Efficient implementation of the continuous-time interaction-expansion quantum Monte Carlo method. *Comput. Phys. Commun.* **252**, 106826 (2019).

Methods

Sample preparation using multianvil press

Ambient oxy-hydroxide samples were purchased from merchant sites (α -FeOOH, purity 99%+, Alfa Aesar, CAS: 20344-49-4 and γ -AlOOH, purity 99%, Macklin CAS: 1318-23-6, natural sample). The purity of

boehmite samples were checked by electron microscope analysis. The result shows boehmite contains 0.03 wt.% of hematite (Supplementary Fig. 4). The powder samples were grounded in an agate motor with alcohol for 1 hour.

High pressure synthesis of ϵ -FeOOH started with grounded goethite powder. The powder was packed in a gold capsule which is rolled in a rhenium heater, and placed in a Kawai-type multi-anvil press at the Geophysical Laboratory, Carnegie Institution of Washington. Synthesis experiments were conducted at 12 or 14 GPa and in the temperature range of 600-1000 °C and kept those conditions for up to 4 hours. Since ϵ -FeOOH is heated to dehydrate even upon Raman laser, the recovered products were characterized by x-ray diffraction (Supplementary Fig. 5 and 6). The grain size of ϵ -FeOOH is around 50 μm (Supplementary Fig. 7). We varied our experimental P - T conditions to constrain the stability fields of ϵ -FeOOH up to 14 GPa (Fig. 1). δ -AlOOH sample was synthesized in a Kawai-type multi anvil press available at Jilin University. The starting composition is $\text{Al}(\text{OH})_3$ and the sample was sealed in a platinum capsule during synthesis. The synthesis was performed at 18 GPa and 900 °C, and then held for 2 hours. We measured the Raman spectroscopy of the synthesized sample to confirm that the product is pure.

***In situ* high-pressure EC measurements using impedance spectroscopy**

High-pressure EC experiment was performed by a Solartron-1260 AC impedance spectroscopy with frequencies between 0.1 Hz and 10 MHz incorporation with a 300- μm anvil culet symmetrical-style DAC. A T-301 steel gasket was pre-indented to a thickness of 50 μm then a hole with diameter $d = 280 \mu\text{m}$ was drilled at the center of the indentation and filled in the mixed powder of boron nitride-epoxy. The filled hole was then compressed to ~ 15 GPa. Afterwards, a 100- μm hole was drilled at the center to act as the insulating sample chamber. Four Pt foils were chosen serving as the electrodes with a thickness of less than 4 μm , which can determine the resistivity of an arbitrary-shaped sample with an even thickness and minimize the resistivity effect from the contact resistance (Supplementary Fig. 8). To avoid impurities and ensure good electrode contact, no pressure medium was used for the EC measurement.

The thickness (t) of the sample in Table 2 was estimated using a simple interpolation method⁶⁴. We compressed a few standard samples to different pressures ($P = 0, 10, 20, 30, 40, 50$ GPa respectively) and calibrated the gasket thickness by a Vernier caliper. The sampling results were fitted to a parabolic relation between pressure and gasket thickness. We calculated the thickness shrinkage rate as the slope ($\delta_t = dt/dP$) of parabolic relation. Using the same gasket material and sample assemblage, the thickness at arbitrary pressure is interpolated by the formula:

$$t(P) = t_{\min} + P \cdot \delta_t$$

where t_{\min} is the thickness of the gasket when pressure is fully released in the experiment run. The thickness of the sample is comparable to that of the gasket. The error in thickness includes measured and systematic error, which is estimated to be about 20%.

First principles simulation based on DFT+DMFT

We first relaxed the crystal structure of ϵ -FeOOH using conventional DFT. The simulation was performed by Quantum Espresso version 6.3 (ref.⁶⁵). The kinetic energy cutoff is 70 Ry for wavefunctions and 600 Ry for charge density. Both lattice parameters and atomic positions were relaxed to the target pressures. We noticed the crystal structure has symmetric hydrogen bonding at 50 GPa.

To proceed with the electronic structure calculation, we used the DFT + DMFT method as was implemented in the DCore code. A noninteracting GGA Hamiltonian, which includes the Fe 3*d* and O 2*p* states, was constructed by the Wannier function projection⁶⁶. The quantum impurity problem was handled by a continuous-time hybridization expansion solver from TRIQS/cthyb^{67,68}. The calculation is performed by DCore version 2.1⁶⁹. We used the same set of Coulomb parameters ($U = 6$ eV and $J_H = 0.89$ eV) for all the structures⁴⁷. All calculations were performed at inverse temperature $\beta = 40$ eV⁻¹ (~ 290 K).

Figures

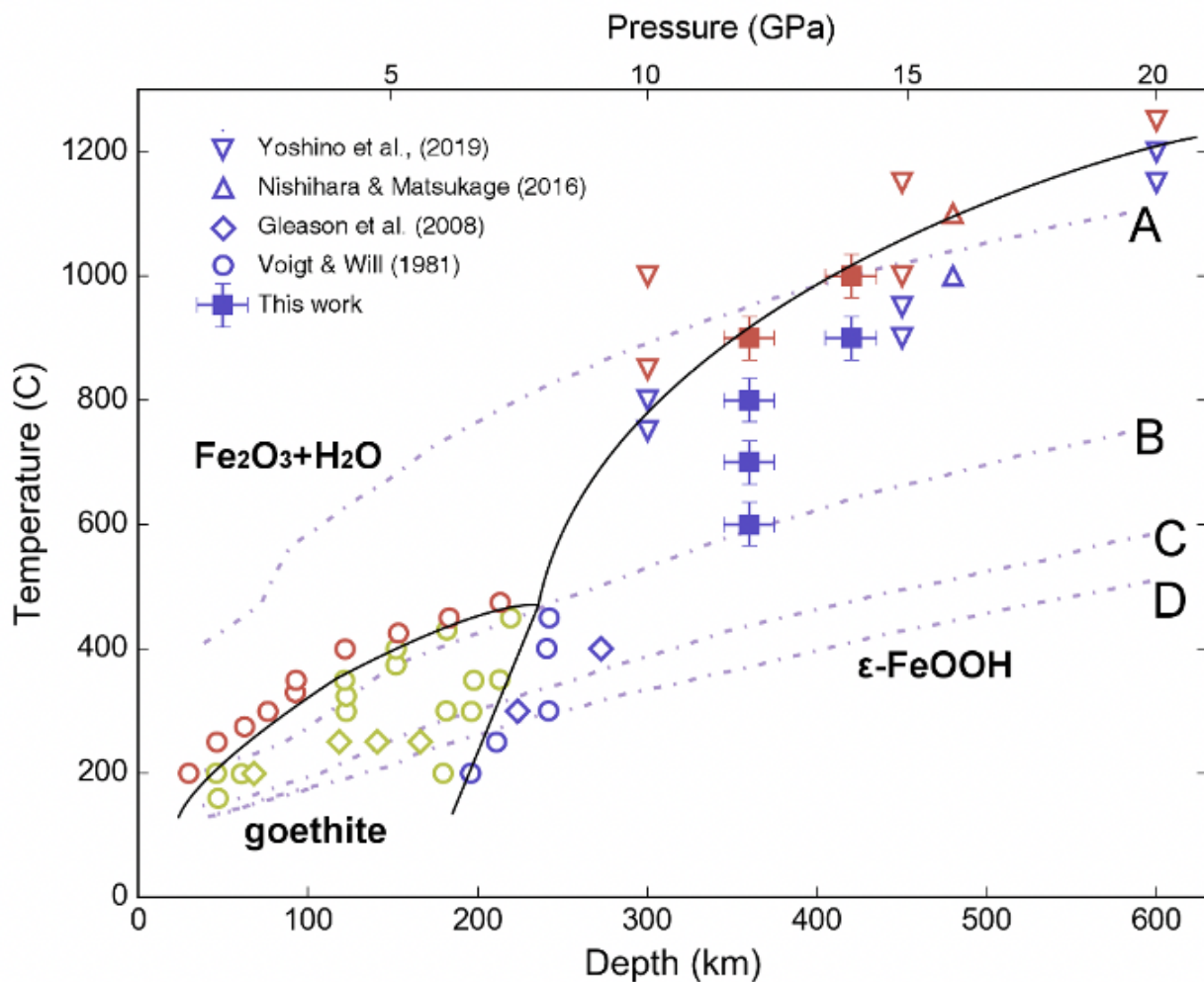


Figure 1

Stability fields of FeOOH. Colors of red, blue and yellow correspond to Fe₂O₃+H₂O, ε-FeOOH and α-FeOOH. Dot dashed curves are thermokinetic model results of four slabs representing subducting lithosphere in different trenches by Kirby et al.³². From A to D, slabs are older and faster sinking.

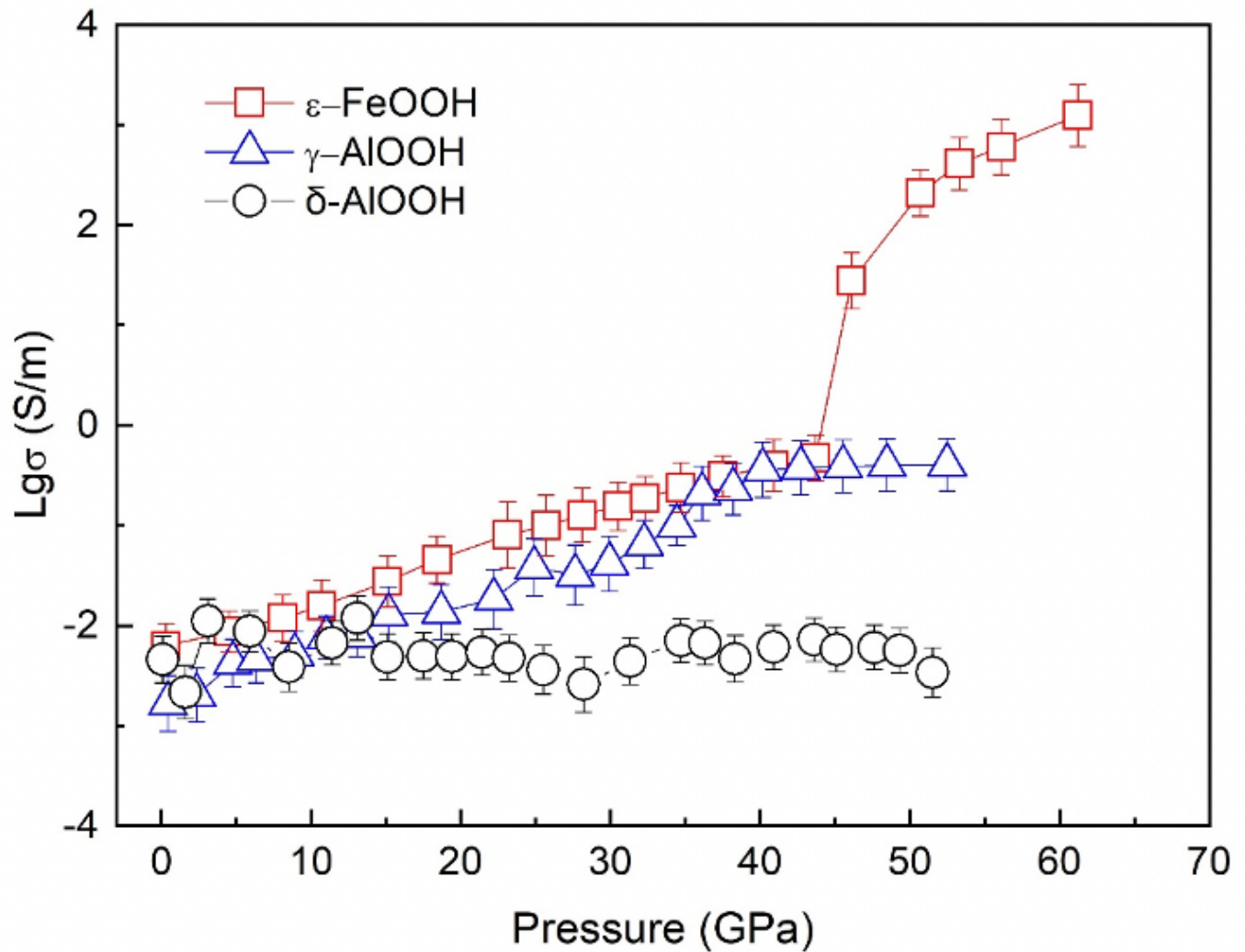


Figure 2

Electrical properties of ε-FeOOH, γ-AlOOH and δ-AlOOH versus pressure at ambient temperature. The EC of ε-FeOOH showed a huge jump at ~45 GPa. The errors were estimated to be ~15%.

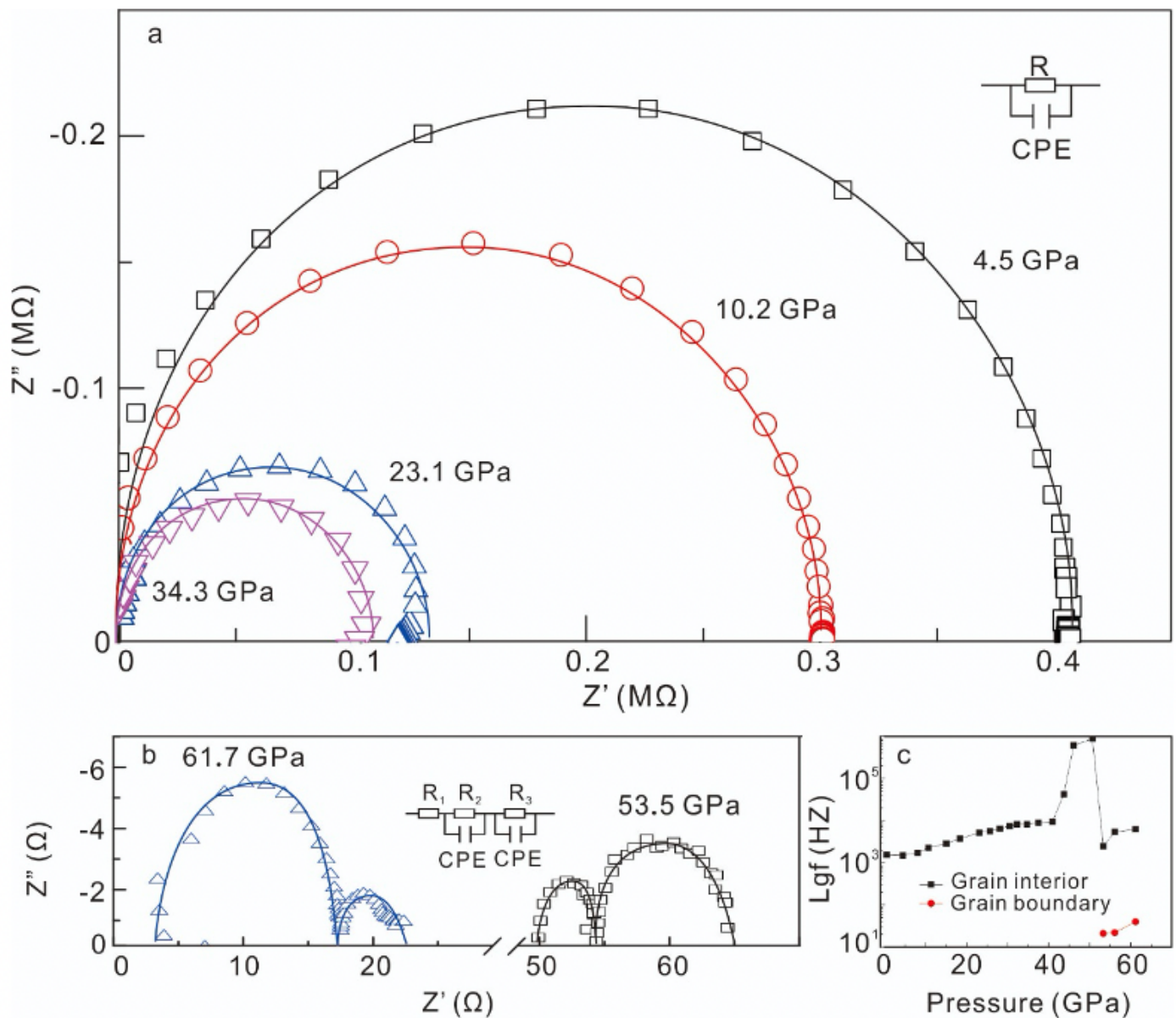


Figure 3

Selected Nyquist plots of ϵ -FeOOH. The solid curves were the corresponding fitting curves with equivalent circuits showed at the corner or top of the figure. a, below 50 GPa the equivalent circuit consists of a single part of one resistor and one constant phase element (R-CPE) in parallel; b, At 53.5 GPa the equivalent circuit splits into three parts. c: Pressure dependence of relaxation frequency for the grain interior and the grain boundary of compressed ϵ -FeOOH.

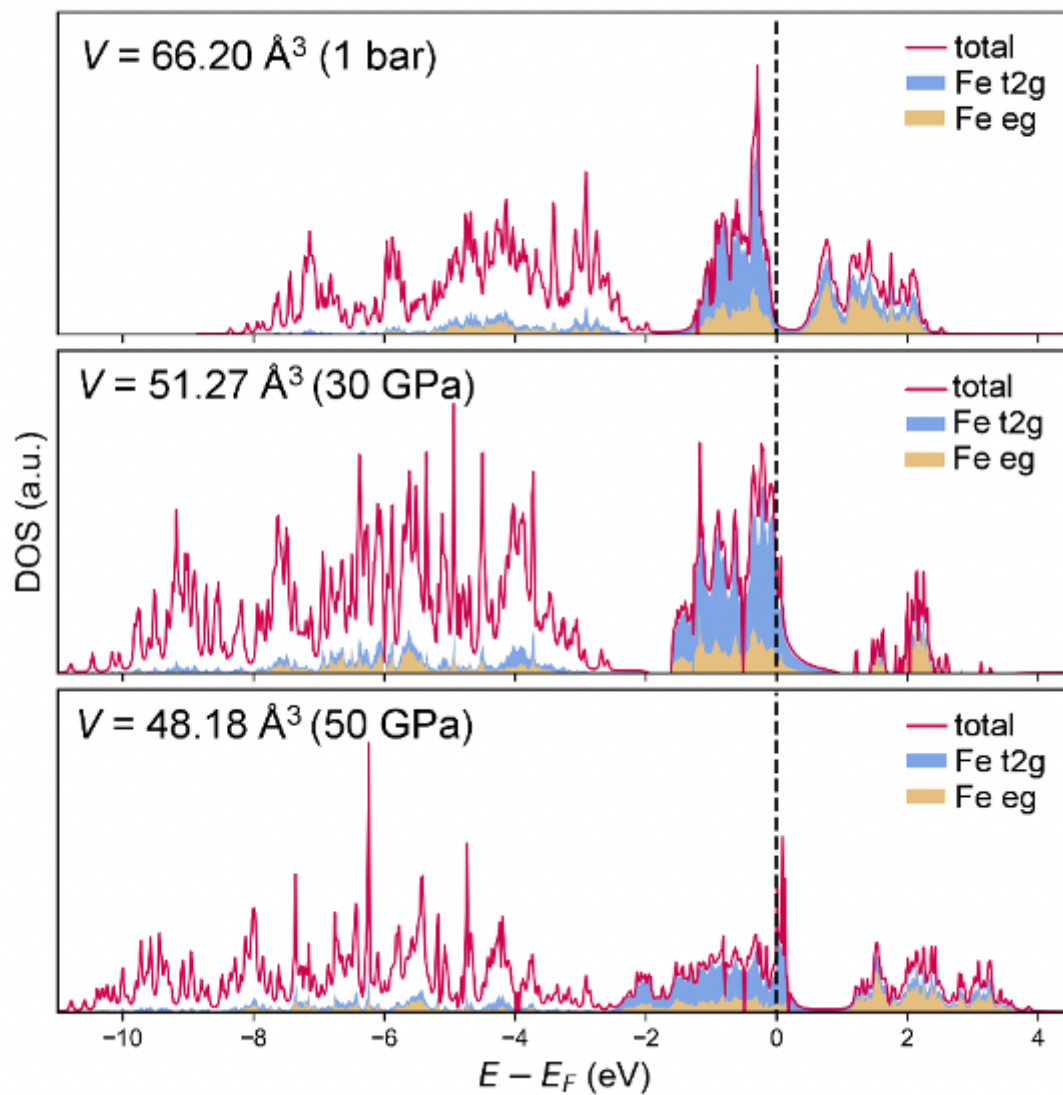


Figure 4

Density of state (DOS) of ϵ -FeOOH at various volumes. Projected DOS of Fe t2g and eg orbitals are plotted in shaded color. At 50 GPa, ϵ -FeOOH is a correlated metal.

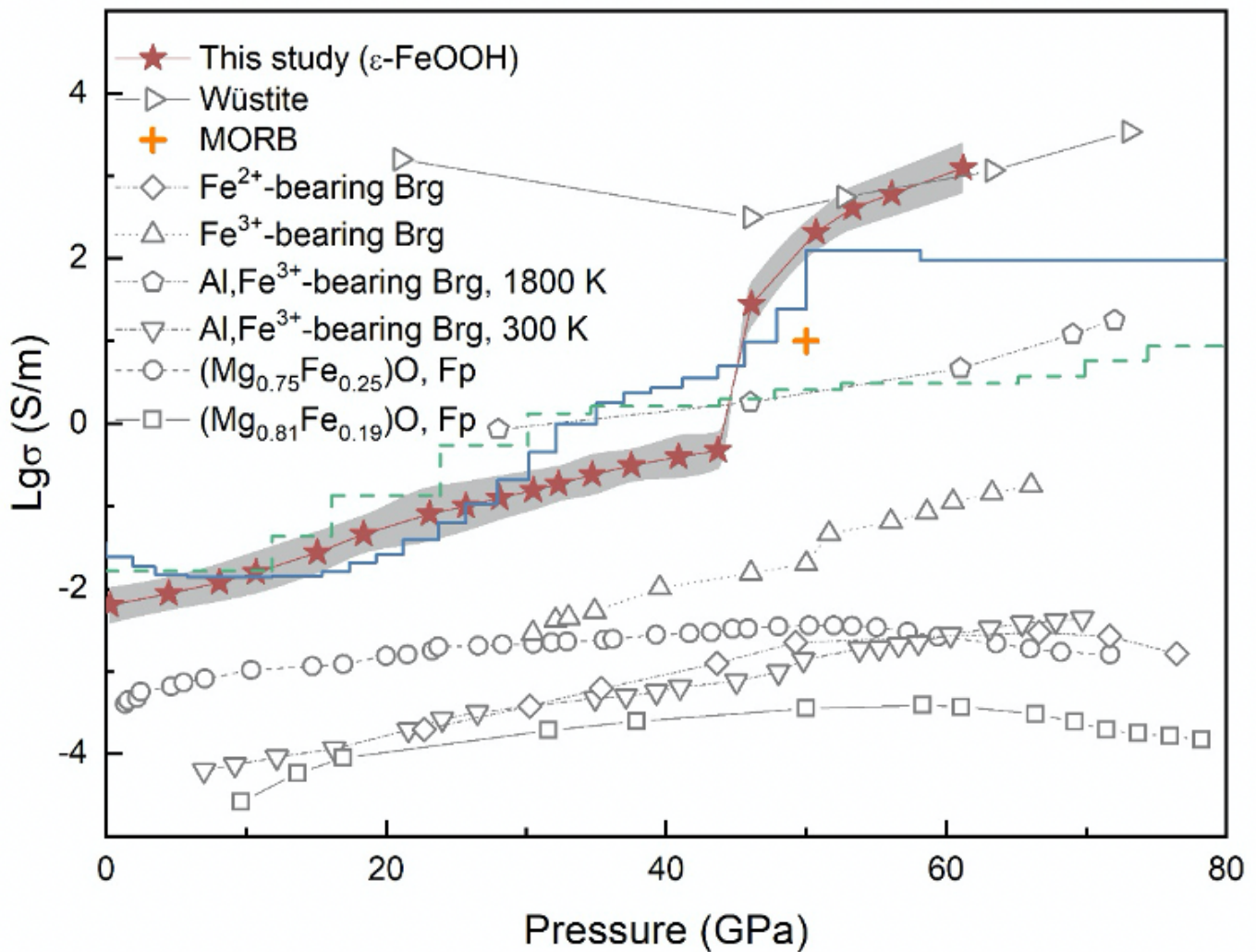


Figure 5

Pressure dependence of the EC in lower mantle phases compared with geomagnetic measurements. Solid asterisk: ϵ -FeOOH at 300 K by this study. Diamond: $(\text{Mg}_{0.9}\text{Fe}_{0.1})\text{SiO}_3$, Fe-bearing Brg at 300 K⁵⁴. Up-pointing triangle: $(\text{Mg}_{0.46}\text{Fe}_{3+0.53})(\text{Si}_{0.49}\text{Fe}_{3+0.51})\text{O}_3$, Fe-bearing Brg at 300 K⁵⁵. Pentagon: $\text{Mg}_{0.83}\text{Fe}_{0.21}\text{Al}_{0.06}\text{Si}_{0.91}\text{O}_3$, Al,Fe-bearing Brg at 1800 K¹³. Down-pointing triangle: $\text{Mg}_{0.83}\text{Fe}_{0.21}\text{Al}_{0.06}\text{Si}_{0.91}\text{O}_3$, Al,Fe-bearing Brg at 300 K¹³. Circle: $(\text{Mg}_{0.75}\text{Fe}_{0.25})\text{O}$ at 300 K¹⁴. Square: $(\text{Mg}_{0.81}\text{Fe}_{0.19})\text{O}$ at 300 K⁵³. Right-pointing triangle: FeO, wüstite at 300 K⁵⁶. Cross: MORB at 1430-2100 K⁵¹. Blue and green line show geomagnetic observed high and average electrical 1D conductivity profile by Constable and Constable¹¹ and Ohta et al.⁵¹, respectively. The gray area is 95% confidence interval.

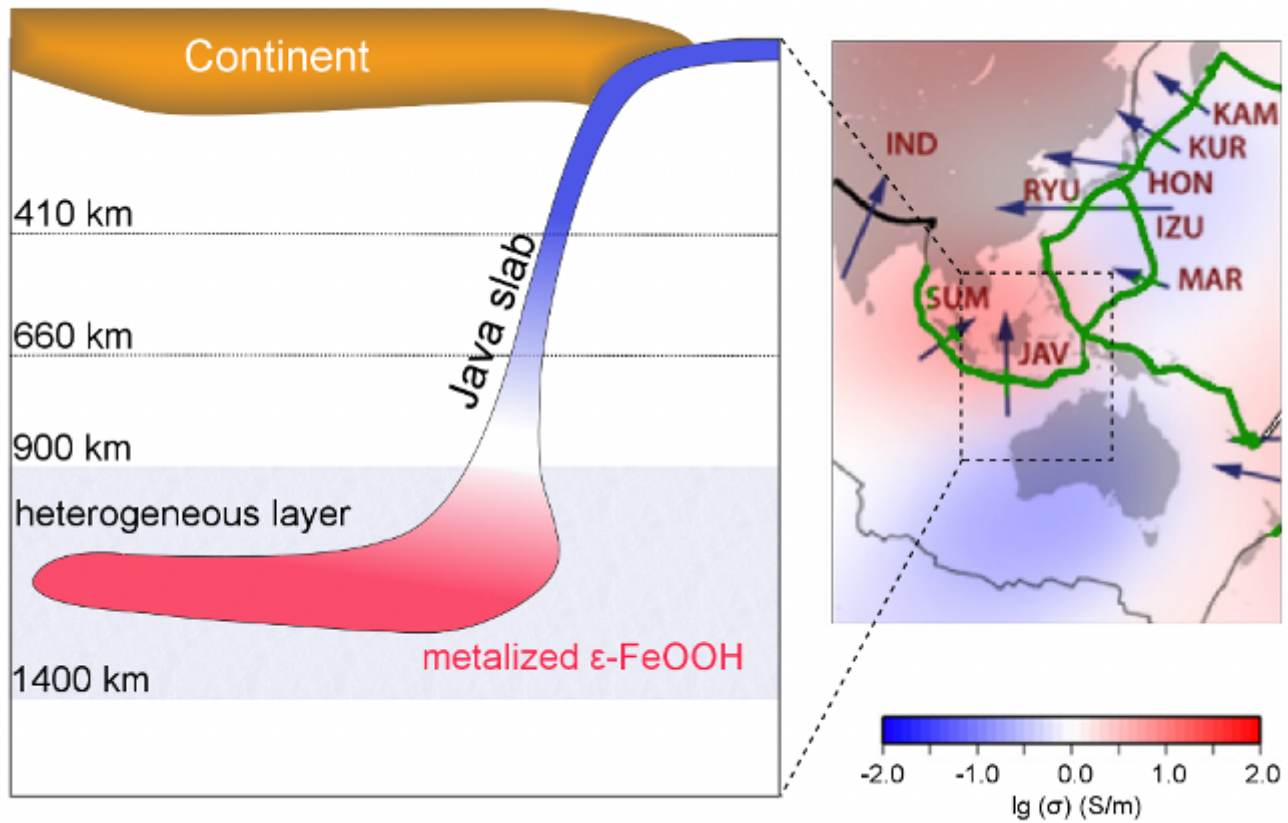


Figure 6

The ϵ -FeOOH origin of heterogeneous EC layer. Left panel zoom in the Java subduction slab (JAV), whose curvature is from Goes et al.⁵⁷. Right panel is an interpolated 3D EC map taken at 1220 km depth⁵. The green curves are the edge of tectonic plates. While the subduction zones on the right panel are: RYU-Ryukyu, IZU-Izu, HON-Honshu, KUR-Kuriles, KAM-Kamchatka, IND-India, MAR-Marianas, SUM-Sumatra.

Supplementary Files

This is a list of supplementary files associated with this preprint. Click to download.

- [Supplementaryinformation.docx](#)